Received: 15 February 2022 | Revised: 8 July 2022 | Accepted: 25 July 2022

DOI: 10.1002/hyp.14672

RESEARCH ARTICLE

WILEY

Subsurface permeability contrasts control shallow groundwater flow dynamics in the critical zone of a glaciated, headwater catchment

Joshua R. Benton[1,2] | Kevin J. McGuire[3] | Madeline E. Schreiber[1]

[1]Department of Geosciences, Virginia Tech, Blacksburg, Virginia, USA

[2]North Carolina Geological Survey, Swannanoa, North Carolina, USA

[3]Department of Forest Resources and Environmental Conservation and Virginia Water Resources Research Center, Virginia Tech, Blacksburg, Virginia, USA

Correspondence
Madeline E. Schreiber, Department of Geosciences, Virginia Tech, Blacksburg, VA 24061 USA.
Email: mschreib@vt.edu

Funding information
Department of Geosciences at Virginia Tech; NSF Division of Environmental Biology Hubbard Brook LTER program, Grant/Award Number: 1637685; National Science Foundation Division of Earth Sciences, Grant/Award Number: 1643327

Abstract

Groundwater flow direction within the critical zone of headwater catchments is often assumed to mimic land surface topographic gradients. However, groundwater hydraulic gradients are also influenced by subsurface permeability contrasts, which can result in variability in flow direction and magnitude. In this study, we investigated the relationship between shallow groundwater flow direction, surface topography, and the subsurface topography of low permeability units in a headwater catchment at the Hubbard Brook Experimental Forest (HBEF), NH. We continuously monitored shallow groundwater levels in the solum throughout several seasons in a well network (20 wells of 0.18–1.1 m depth) within the upper hillslopes of Watershed 3 of the HBEF. Water levels were also monitored in four deeper wells, screened from 2.4 to 6.9 m depth within glacial drift of the C horizon. We conducted slug tests across the well network to determine the saturated hydraulic conductivity (K_{sat}) of the materials surrounding each well. Results showed that under higher water table regimes, groundwater flow direction mimics surface topography, but under lower water table regimes, flow direction can deviate as much as 56 degrees from surface topography. Under these lower water table conditions, groundwater flow direction instead followed the topography of the top of the C horizon. The interquartile range of K_{sat} within the C horizon was two orders of magnitude lower than within the solum. Overall, our results suggest that the land surface topography and the top of the C horizon acted as end members defining the upper and lower bounds of flow direction variability. This suggests that temporal dynamics of groundwater flow direction should be considered when calculating hydrologic fluxes in critical zone and runoff generation studies of headwater catchments that are underlain by glacial drift.

KEYWORDS
critical zone, flow direction, glaciated catchment, groundwater, hydraulic gradient, subsurface permeability

1 | INTRODUCTION

In the critical zone of headwater catchments, shallow groundwater flow is particularly important as it influences runoff generation (Haught & Tromp-van Meerveld, 2011; Penna et al., 2015), the connectivity between hillslopes and streams (Detty & McGuire, 2010b; Emanuel et al., 2014; Inamdar & Mitchell, 2007; Singha & Navarre-Sitchler, 2022), nutrient transport (Stieglitz et al., 2003; van Verseveld et al., 2009) and pedogenic processes within catchment soils (Bailey et al., 2019; Twidale, 1990). As a result, many of the chemical and physical characteristics of headwater streams are intrinsically connected to the critical zone of their surrounding catchment by shallow groundwater flow paths that deliver water and solutes from the hillslopes to the stream network. Therefore, predicting the physical and chemical response of headwater catchments to both land disturbances and changes in climate requires accurate measurement of the magnitude and direction of shallow groundwater flow.

Despite the importance of shallow groundwater in headwater catchments, characterization is challenged by the spatial and temporal variability in groundwater flow. First, groundwater basins are often delineated using land surface topography, under the assumption that groundwater drainage follows surface topography. This assumption can lead to significant error in water-budget calculations if groundwater basin divides do not correspond to land surface divides (Hinton et al., 1993). Land surface digital elevation models (DEMs) are commonly used for estimating groundwater flow direction at the catchment scale, and the resolution of DEMs can have a significant impact on inferred catchment boundaries and drainage areas, particularly in low-order stream basins (Erdbrügger et al., 2021). In addition, microtopography has been shown to influence groundwater flow. For example, Frei et al. (2010) found that inclusion of microtopography in 3D numerical modelling of runoff dynamics in the riparian wetland of a small, headwater stream was able to reproduce the observed nonlinear, hysteretic relationship between water table elevations and stream discharge. Using a 2D analytical flow model, Bresciani et al. (2016) demonstrated that microtopographic low-points constrain the upper limits on water table fluctuations and therefore control groundwater flow when water tables intersect these points. Together, these previous studies show a complex interaction of water table elevation and surface topography on groundwater flow paths, underscoring the importance of making physical measurements of the water table surface.

Shallow groundwater flow in headwater catchments can be highly dynamic or transient, influenced by storm and snowmelt events and other impacts on water table elevations that are only elucidated with high-frequency measurements in well networks (Haught & Tromp-van Meerveld, 2011; Smith et al., 2014; Zimmer & McGlynn, 2017). For example, Detty and McGuire (2010a) found that water tables within the soil zone of a glaciated, headwater catchment were often transient (persisting seasonally or on an event basis) and responded nonuniformly to recharge events depending upon landscape position and antecedent conditions. Rodhe and Seibert (2011) and von Freyberg et al. (2014) observed significant variability of shallow groundwater flow direction within riparian soils in a glaciated catchment. During storm events with high-water tables, the groundwater flow direction was perpendicular to the direction of stream flow (flowing towards the stream) while during nonstorm periods under lower water tables, flow direction was parallel to it. These studies show that abrupt shifts in hydrologic regimes and connectivity between hillslopes and streams can occur over short time-periods (event time-scales), thus underscoring the importance of high-frequency measurements to adequately characterize groundwater flow within headwater catchments.

A significant portion of northern North America, Europe and Asia is mantled by glacial sediments (Yager et al., 2019). Headwater catchments in these areas have developed in glacial parent materials since deglaciation through physical and chemical weathering and soil forming processes. Consequently, shallow groundwater dynamics in headwater, glaciated catchments are influenced by the structure and permeability of the complex glacial deposits and permeability contrasts between different soil horizons or depths (Blumstock et al., 2016; Gannon et al., 2014; Maier et al., 2020). For example, in a hillslope study underlain by a compacted glacial till, Hutchinson and Moore (2000) found that hydraulic gradients in shallow soil followed the topography of the underlying lower-permeability glacial till. Other studies in glacial settings have shown that soil physical properties can vary with depth and influence groundwater flow (e.g., Hinton et al., 1993; Nyberg, 1995; Shanley et al., 2003). In till-mantled headwater catchments, hydraulic conductivity of the solum material (O, A, E, B horizons) has been shown to decrease exponentially with depth, with the most significant decrease between the solum and C horizon (Burns, 2012; Detty & McGuire, 2010a; Harpold et al., 2010; Kendall et al., 1999; Maier et al., 2021; Shanley et al., 2003). These permeability contrasts between the solum and C horizon can occur within the uppermost meter of the subsurface, suggesting that shallow groundwater flow dynamics in these glacial catchments may be particularly sensitive to critical zone architecture. However, to date, few catchment studies have addressed the influence of permeability contrasts on the dynamics of groundwater flow in glacial settings.

In this study, we investigated the influence of permeability contrasts between the solum and C horizon and how the subsurface topography of the C horizon affects local (i.e., 5–10 m scale) hydraulic gradients and groundwater flow direction in a glaciated headwater catchment. To do this, we used high-frequency measurements (1–10 min) of water-table elevations recorded by wells installed within three hillslope transects in the Hubbard Brook Experimental Forest (New Hampshire) over a 10-month period. We combined high-frequency water-table measurements with measurements of hydraulic conductivity and estimated elevations and thicknesses of soil horizons to determine if shallow groundwater flow direction and magnitude vary through time in the critical zone of this glaciated headwater catchment. We also evaluated the drivers influencing the variability of shallow groundwater flow direction.

2 | METHODS

2.1 | Site description

We conducted this study in Watershed 3 (WS3), a south-facing, 42 ha gauged watershed within the Hubbard Brook Experimental Forest (HBEF) in Woodstock, NH (Figure 1). WS3 encompasses the headwaters for Paradise Brook, a perennial first-order headwater stream (Hooper & Shoemaker, 1986; Zimmer et al., 2013). WS3, with an elevation range of 205 m and an average slope of 28% (Likens, 2013), is the hydrologic reference watershed for a series of paired watershed vegetation removal experiments (Hornbeck et al., 1970) designed to study headwater streamflow response to deforestation (Likens et al., 1970). As the reference, WS3 was left relatively undisturbed, has not been logged since late 1910s and has maintained an approximate steady-state biomass since the 1980s (Likens, 2013). The Hubbard Brook Valley is covered by a northern hardwood forest comprised of American Beech (*Fagus grandifolia*), sugar maple (*Acer saccharum*) and yellow birch (*Betula alleghaniensis*) dominating deeper soils and better drained sites, and balsam fir (*Abies balsamea*), red spruce (*Picearubens*) and white birch (*Betula papyrifera* var. *cordifolia*) dominating shallow soils and wetter sites (Likens, 2013). The climate of WS3 is classified as humid continental with a mean annual precipitation of 140 cm evenly distributed throughout the year. Approximately one-third to one-quarter of this precipitation occurs as snowfall (Bailey et al., 2003).

The geology within WS3 consists of metasedimentary sillimanite grade, pelitic schists of the upper Rangeley Formation (Bailey et al., 2019) that are overlain by glacial drift of varied thickness deposited during Wisconsin glaciation in the late Pleistocene (Bailey et al., 2014) (Figure 1b). The glacial drift is primarily derived from local granites and schists (Bailey et al., 2003) that may be up to 10 m thick in the central to upper portions of WS3 and is thin and interspersed with exposed bedrock along the catchment divides (Bailey et al., 2019). Portions of basal till have been reworked by glacial melt waters, producing coarse lenses with lower bulk density and higher concentrations of sand and boulders, resulting in a spatially heterogenous permeability architecture (Bailey et al., 2014).

In this study, we separated the soil into 1) the solum, as the surficial portion of glacial drift that has undergone weathering and soil forming processes and 2) the C horizon, as the less altered drift (i.e., parent material) underlying the solum (Figure 1b). The solum encompasses all the soil horizons above the C horizon (O, A, E, B), although all horizons are not always present. The transition between the solum and the C horizon at Hubbard Brook is often a gradational contact producing a transitional soil horizon (BC horizon) that exhibits properties of both the B and C horizons.

Soils, where not confined by shallow bedrock, average 0.5–0.7 m to the top of the C horizon and are characterized predominantly as Spodosols, formed primarily through podzolization (Bailey et al., 2019; 2014). Soil development at HBEF has both a lateral and vertical component, leading to predictable spatial patterns of soil variation across different landscape positions (Bailey et al., 2014). For example, within

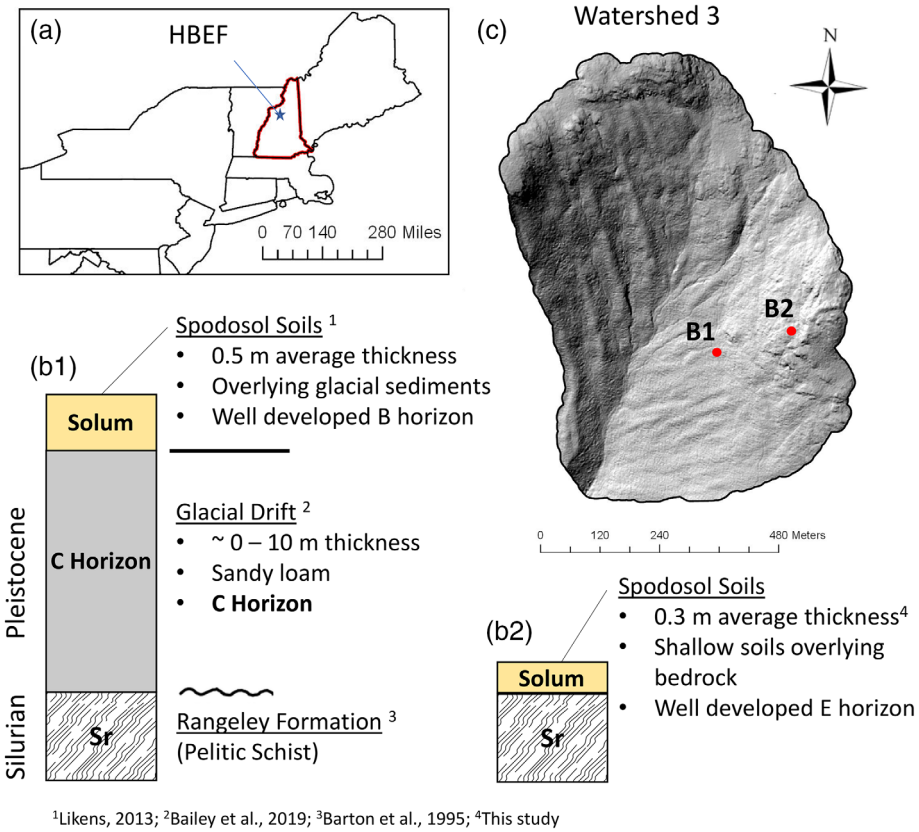

[1]Likens, 2013; [2]Bailey et al., 2019; [3]Barton et al., 1995; [4]This study

FIGURE 1 (a): Map showing the location of the Hubbard brook experimental Forest and watershed 3. (b): Stratigraphic columns (not drawn to scale) showing the surficial deposits overlying bedrock at two example locations (B1 and B2) within watershed 3. At location B1, typical of lower elevations of WS3, Pleistocene glacial drift comprising the C horizon sit unconformably on top of the fractured, crystalline bedrock of the Rangeley formation, and the solum is the weathered portion of the glacial drift that has undergone significant alteration as a result of soil-forming processes. At location B2, typical of higher elevations and the divides of the catchment, the solum consists of shallow organic rich soils with well-developed E horizons directly overlying bedrock. (c): Lidar-derived hillshade digital elevation model (DEM) of watershed 3 highlighting the drainage network, and the variation in topography across the catchment. The east-facing slope has well defined valleys and ridges while the west-facing slope has a more planar topography.

the upper elevation portions of the catchment, particularly in convergent zones adjacent to bedrock outcrops, soils have a thicker E horizon relative to other horizons; further downslope, however, soils tend to have thicker B horizons relative to other horizons. These distinct soil morphological units have been identified and mapped within WS3 (Bailey et al., 2019; Gillin et al., 2015). Gannon et al. (2014) showed that these soil units correlate with distinct water-table regimes and exhibit different threshold subsurface stormflow responses to changes in catchment storage.

2.2 | Well network

The monitoring well network for this study consisted of 24 wells along three hillslope transects (Figure 2: Transects 42, 52 and 86). Transects 42 and 52 were at higher elevations on the east facing slope, 713–667 meters above mean sea level (MASL); transect 86 was on the west facing slope, at a lower elevation (604–618 MASL). The well network contained 20 shallow wells (0.18–1.1 m depth) screened within the solum, and 4 deep wells (2.4–6.9 m depth) screened within the C horizon (Figure 2). At higher elevations, shallow wells were installed within the E horizon directly overlying bedrock (Figure 1b), and at lower elevations shallow wells were installed within the B horizon that directly overlies the C horizon (Figure 1a) or the transitional BC horizon. An example cross-section of a well transect illustrates the transition from the upslope bedrock dominated portions of WS3 to the downslope thickening wedge of glacial sediments comprising the C horizon (Figure 3).

Within the shallow well network, there were five well clusters of three wells per cluster used for determining the magnitude and direction of the hydraulic gradient. The wells within each cluster were spaced near each other (within 8 m) to minimize the risks of measuring hydrologically disconnected water-tables within an aquifer that is dissected by irregularly undulating bedrock topography. The well network was surveyed with a total station theodolite at 1 mm ± 1 ppm measurement accuracy. The properties of wells and well clusters are summarized in Table 1.

2.3 | Identification of soil horizons

Soil horizons were identified using a combination of auger cuttings and soil pits. During installation of wells, auger cuttings were examined to identify soil horizons. Soil horizons were identified by a combination of properties (Munsell colour, texture, structure and root density) consistent with methods used in previous work at Hubbard Brook (Bailey et al., 2014). The C horizon is typically distinguished from the solum by having a coarser texture, lighter hue of 2.5 Y, and lack of roots while the overlying B horizon typically has a darker hue (7.5–10 YR), finer texture, and a greater density of roots. As a transitional horizon, the BC horizon underlies the B horizon, typically has a hue of 10 YR, and exhibits properties of both the B and C horizon. A

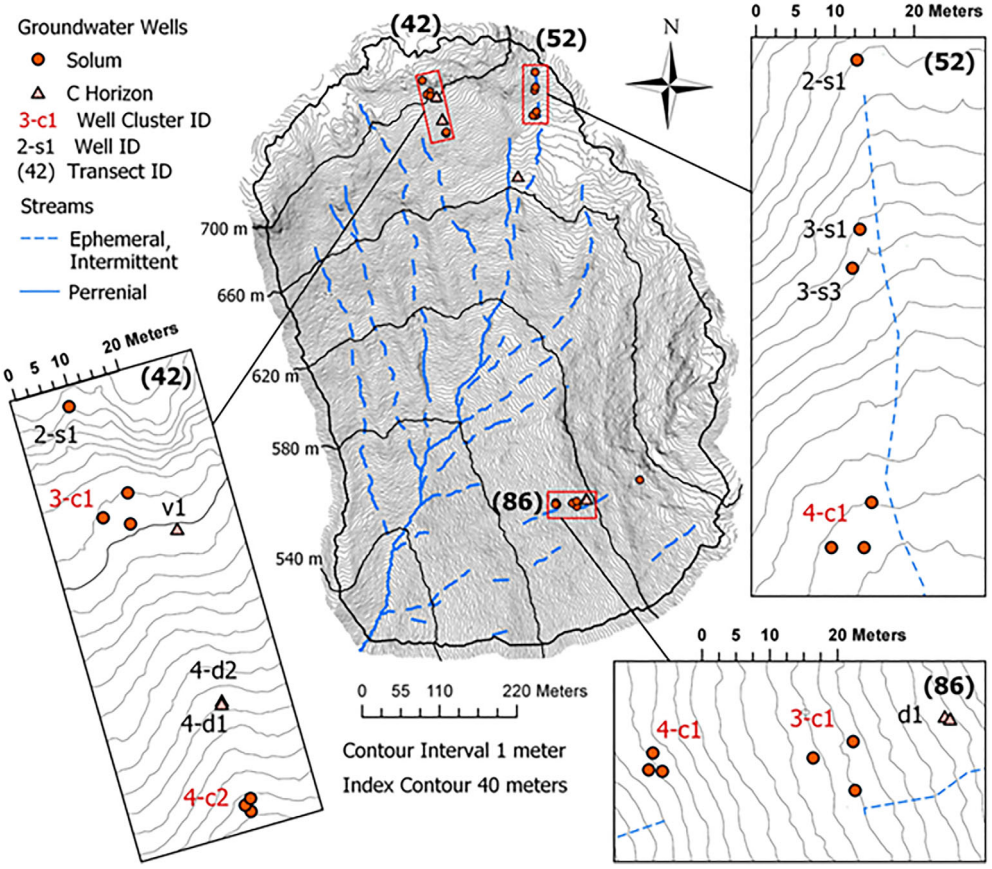

FIGURE 2 A topographic map of WS3 with the locations of each well transect (42, 52 & 86) where wells are symbolized by the stratum in which the screened interval is installed in. Shallow wells are installed within the solum (circles); deeper wells are installed within the C horizon (triangles). The location of the barometric logger is at the top of a deep well at (86)-B, and the location of the rain gauge is indicated by a green star. The surface drainage network is represented by solid blue lines (perennial streams) and dashed blue lines (intermittent & ephemeral streams).

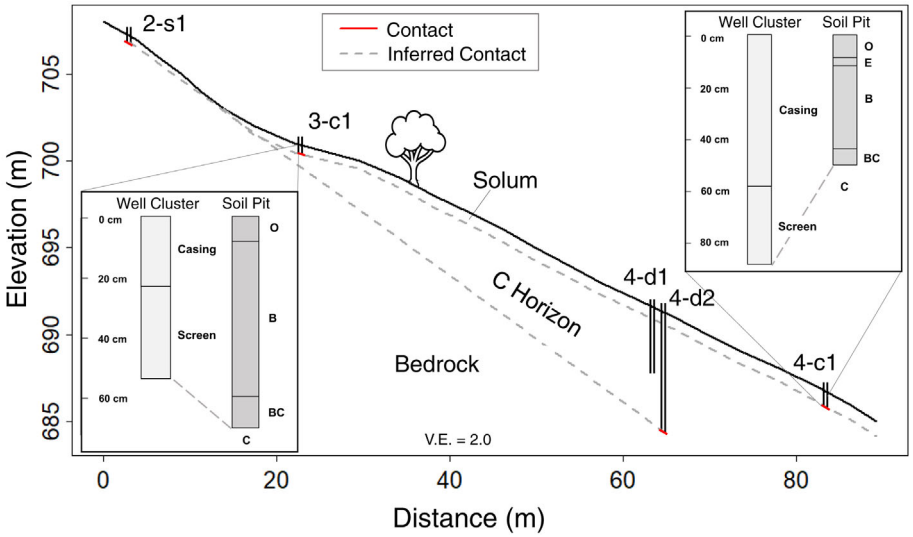

FIGURE 3 A cross-section of transect 42 with the locations and depths of select wells, and contacts between bedrock, C horizon and the solum. Well 2-s1 is installed within the solum directly overlying bedrock. The insets show the well construction information at 3c-1 and 4-c1 (see Figure 2 for locations) compared with the horizon thicknesses measured within the nearest soil pit.

TABLE 1 Well construction details, including screen length (m), screen depth (m from land surface), screened horizon, and the ID of the well cluster.

Well ID	Screen length (*m*)	Screen depth (*m*)	Screened horizon	Well cluster ID
(42)-2-s1	0.15	0.33	E	
(42)-3-s1	0.31	0.46	B	(42)-3-c1
(42)-3-s2	0.31	1.05	B	(42)-3-c1
(42)-3-s3	0.31	0.53	B	(42)-3-c1
(42)-3-d1	0.31	2.67	C	
(42)-4-s1	0.31	0.84	B	(42)-4-c1
(42)-4-s2	0.31	0.88	B	(42)-4-c1
(42)-4-s3	0.31	0.91	B	(42)-4-c1
(42)-4-d1	0.61	6.86	Bedrock surface	
(42)-4-d2	0.61	3.71	C	
(52)-2-s1	0.15	0.37	E	
(52)-3-s1	0.31	0.56	B	
(52)-3-s3	0.31	0.51	B	
(52)-4-s1	0.31	0.46	B	(52)-4-c1
(52)-4-s2	0.31	0.63	B	(52)-4-c1
(52)-4-s3	0.31	0.79	B	(52)-4-c1
(52)-4-d2	0.61	3.05	Bedrock surface	
(86)-3-s1	0.31	0.77	B	(86)-3-c1
(86)-3-s2	0.31	0.57	B	(86)-3-c1
(86)-3-s3	0.31	0.74	B	(86)-3-c1
(86)-3-d2	0.61	3.05	Bedrock surface	
(86)-4-s1	0.31	0.97	BC	(86)-4-c1
(86)-4-s2	0.31	0.70	BC	(86)-4-c1
(86)-4-s3	0.31	0.69	BC	(86)-4-c1

more detailed description of soil horizons presented within this study can be found in Bailey et al. (2014). In addition, adjacent to each well cluster, soil pits were hand dug to allow for a detailed description and measurement of soil horizon depths and thicknesses. These data were used in conjunction with the auger cuttings to determine the soil horizon surrounding the screened interval (Table 1).

At the larger scale, an auger investigation was conducted to identify the presence and thicknesses of soil horizons in each subcatchment. Data from this investigation were used for determining the gradient and slope direction of the top of the C horizon compared to the land surface across each subcatchment. The auger investigation was conducted along multiple, equally spaced transects creating a grid

with a 10-meter spatial resolution. Each auger investigation went to depth of refusal, and the depths of soil horizon transitions were measured including the depth to the top of the C horizon (if the C horizon was present). The GPS locations of transect endpoints were determined using a Trimble Geoexplorer XT GPS unit with an external hurricane antenna; the GPS locations of each auger point were extrapolated from endpoint measurements. Auger locations where the C horizon was not observed were filtered from the dataset leaving a total of 30 measurements in transect 52, 37 measurements in transect 42, and 15 measurements in transect 86 used for gradient calculations of the C horizon. Within ArcGIS, a series of three-point clusters of comparable size and geometry to the well clusters were identified, and the maximum slope directions of the ground surface and the top of the C horizon were calculated for each cluster.

2.4 | Well construction, installation & development

Details of well construction are shown in Table 1. The shallow wells were constructed using 2-inch diameter solid PVC attached to 2-inch diameter PVC screen (0.010 slot size). The screened interval was 30.5 cm for wells in the B horizon, and 15.2 cm for wells in the E horizon. Wells in the solum were installed using a 3-inch diameter bucket auger. Once the well was seated in place within the borehole, the annular space was backfilled with the filter pack (sand) to approximately 2.5 cm above the top of screened interval. A combination of locally derived sand and industrially sourced silica sand was used for the filter pack. The type of filter pack sand was kept consistent between wells within a given cluster. The locally sourced sand was obtained from quarries in glaciofluvial deposits; the material was sieved to exclude grain size diameters smaller than 0.5 mm (US Standard Sieve #35) and coarser than 2 mm (US Standard Sieve #35). Above the filter pack, the annular space was backfilled with the native soil removed during the borehole excavation. A plastic flange was tightly wrapped around each well and placed at the top of the soil backfill to mitigate surface infiltration and preferential flow around the well.

The deep wells screened within the C horizon were installed using a track-mounted drill rig using hollow-stem augers. Wells were constructed with 2-inch (0.0508 m) PVC and screen (0.010 slot size); the annular space surrounding the well screen was filled with #1 silica sand to approximately 0.2–0.5 meters above the top of the screened interval, and 00 sand to approximately 1 meter above the top of the screened interval. Above this, native material was backfilled above the sand, and bentonite was added to 30–60 cm below surface.

Wells were developed using surging and pumping methods. If the well was dry after installation, stream water was poured into the well and then pumped back out multiple times until the water appeared clear.

2.5 | Measurement of water levels

Pressure transducers (HOBO © Onset U20 & U20L data loggers) were installed within each well to measure water levels at 1-10-min logging intervals. Water level measurements were collected between Mar. 2019 and Jan. 2020. The pressure transducers were suspended immediately above the base of the well by a 20-pound test monofilament line attached to the vented cap of the well. To measure barometric pressure in the watershed, we installed an additional transducer within the PVC casing of one of the deeper wells. Raw pressure data obtained from the transducers were converted to water level by compensating for barometric pressure and reference water level measurements using Onset® HOBOware® graphing and analysis software. The water level dataset is available in Benton et al. (2022).

Manual measurements of the water-table within each well were also collected throughout the study period using a Solinst® water level meter (1/1000 ± 0.01 ft measurement accuracy) prior to installation of the loggers, before the removal of loggers for data retrieval, and during aquifer tests.

2.6 | Measurement of hydraulic conductivity

The saturated hydraulic conductivity of the material surrounding each well was estimated using the Hvorslev method of analysing rising head slug test data (Hvorslev, 1951). The majority of slug tests were conducted in May 2019 when water-tables were relatively high-across the well network. A total of 47 slug tests were conducted across the entire well network, with at least two slug tests conducted for each shallow well.

2.7 | Calculation of hydraulic and topographic gradients

2.7.1 | Magnitude and direction of groundwater hydraulic gradients

Groundwater hydraulic gradients were calculated using R Statistical Software (R Core Team, 2020) using time series of water level elevation combined with the horizontal coordinates of each well, assuming a linear change in head between each well. The hydraulic head (h) within three wells can be expressed as three points on a plane, and a system of linear equations:

where x is the longitudinal coordinate, y is the latitudinal coordinate, and h is the elevation of the water table.

This system of linear equations can be expressed in matrix form with the coefficient matrix (A), variable matrix (B), and the constant matrix (C).

A B C

$$\begin{bmatrix} 1 & x_1 & y_1 \\ 1 & x_2 & y_2 \\ 1 & x_3 & y_3 \end{bmatrix} \begin{bmatrix} a \\ b \\ c \end{bmatrix} = \begin{bmatrix} h_1 \\ h_2 \\ h_3 \end{bmatrix} b = \frac{\partial h}{\partial x}, \; c = \frac{\partial h}{\partial y}$$

$$\mathrm{B} = \mathrm{A}^{-1}\mathrm{C} \tag{1}$$

The unique solution to the system, column vector B, is determined by multiplying the inverse of the coefficient matrix (A^{-1}) by the column

vector C. This yields the hydraulic gradient in the *x*-direction ($\frac{\partial h}{\partial x}$), and the hydraulic gradient in the *y*-direction ($\frac{\partial h}{\partial y}$). The magnitude of flow ($\frac{dh}{dl}$) is then determined with Pythagorean's theorem and the direction of maximum hydraulic gradient (θ) is determined by the inverse tangent function:

$$\frac{dh}{dl} = \sqrt{b^2 + c^2}, \theta = \tan^{-1}\left(\frac{b}{c}\right) \quad (2)$$

To calculate groundwater flow direction, we assumed that groundwater flows in the direction of the maximum hydraulic gradient (θ). Flow direction calculations were made at every time step in which water levels above a minimum threshold were detected within each of the three wells. Flow directions are reported in azimuth defined as degrees clockwise from true north.

2.7.2 | Magnitude and direction of surface and subsurface topographic gradients

The maximum horizontal gradient and the slope direction (direction of maximum horizontal gradient) were determined at each well cluster for the land surface and the top of the C horizon. The maximum gradients of the land surface and the top of the C horizon were calculated by replacing water table elevation (h) in Equation 1 with the elevation of the land surface and the elevation of the top of the C horizon measured at each well location.

2.8 | Calculation of hydrologic fluxes

Hydrologic fluxes through the solum were estimated using Darcy's Law for saturated water flow through a porous medium at each of the well clusters installed at the base of the solum. The hydrologic flux (units of L/T) was calculated by multiplying the arithmetic mean of the saturated hydraulic conductivity (L/T) determined from slug test analyses of that well by the hydraulic gradient (L/L) (Equation 2) at 10-min intervals.

3 | RESULTS

3.1 | Saturated hydraulic conductivity

The range of saturated hydraulic conductivity (K_{sat}) values within the solum spanned two orders of magnitude with a minimum of 1.3×10^{-6} m/s, and a maximum of 1.8×10^{-4} m/s (Figure 7). The K_{sat} values measured within the C horizon were markedly lower than values measured within the solum, exhibiting a range of 5.0×10^{-8} to 1.6×10^{-6} m/s. The interquartile range of K_{sat} within the C horizon (1.5×10^{-7} to 9.8×10^{-7} m/s) was two orders of magnitude lower than the interquartile range of K_{sat} values within the solum (1.6×10^{-5} to 5.1×10^{-5} m/s) (Figure 4). A Mann–Whitney U Test (Stats Package, R Core Team, 2020) showed that K_{sat} values were significantly different between the solum and C horizon with a *p*-value (1.2×10^{-4}) less than the significance value (0.05), implying a difference in K_{sat} between the screened horizons.

K_{sat} measurements from this study were compared with previous studies (Burns, 2012, Detty, 2010) that used slug test methods for estimating K_{sat} within the upper C horizon (<2.5 m of total depth, Figure 5). The relationship between K_{sat} and depth (Figure 8) showed a general exponential decrease in K_{sat} with respect to increasing depth.

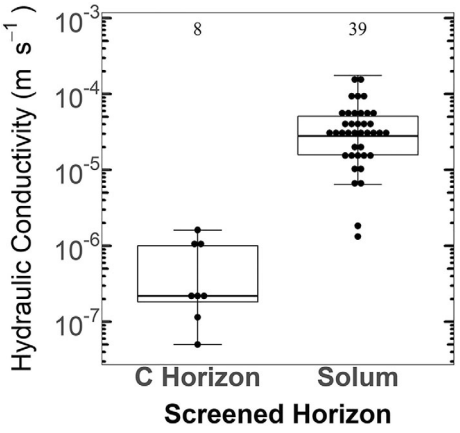

FIGURE 4 Box plots showing saturated hydraulic conductivity (K_{sat}) values measured using slug tests within the B & E horizons (solum) and the C horizon. The number of measurements is shown at the top of the boxplot.

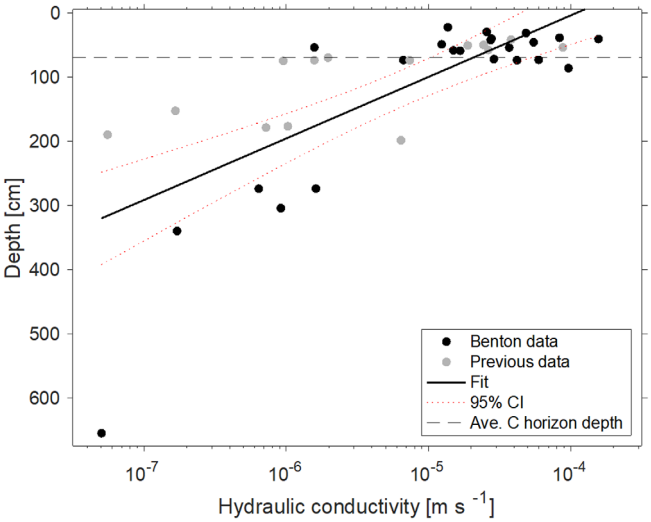

FIGURE 5 The relationship between saturated hydraulic conductivity (K_{sat}) values and depth below land surface. Data from previous work (Burns, 2012; Detty, 2010) is included for comparison. Grey dashed horizontal line reflects the average depth of the C horizon; red dotted line reflects the 95% confidence interval of the linear regression. Note that the x-axis is on a logarithmic scale.

3.2 | Deviations between surface and C horizon topography

The difference between the surface slope direction and the top of the C horizon (ΔGC) determined from the auger investigation in each subcatchment varied between transects. Three examples are included (Figure 6) to illustrate ΔGC patterns across WS3. ΔGC measurements from each well cluster are also included for comparison. Overall, ΔGC had a larger range (±30 degrees) of values compared to the ΔGC variability observed within the well clusters; however, the highest frequency of ΔGC observations from auger investigations showed similar trends to ΔGC observed at each well cluster. For example, the highest frequency of ΔGC measurements within transect 42 ranged between ±10 degrees within a slightly positive skew and ΔGC observed within the well clusters also ranged between ±10 degrees. In transect 86, the majority of ΔGC measurements were negative, and both ΔGC measurements within the well clusters were also negative. Finally, in transect 52, ΔGC measured at the well cluster coincided with the larger frequency of ΔGC values derived from the auger investigation.

3.3 | Water table characteristics and response to recharge events

Throughout the study period (Mar. 2019–Jan. 2020), water tables were transient within the shallow wells (Figure 7a–d), rising in and out of the solum, and were permanent within the deeper wells, fluctuating

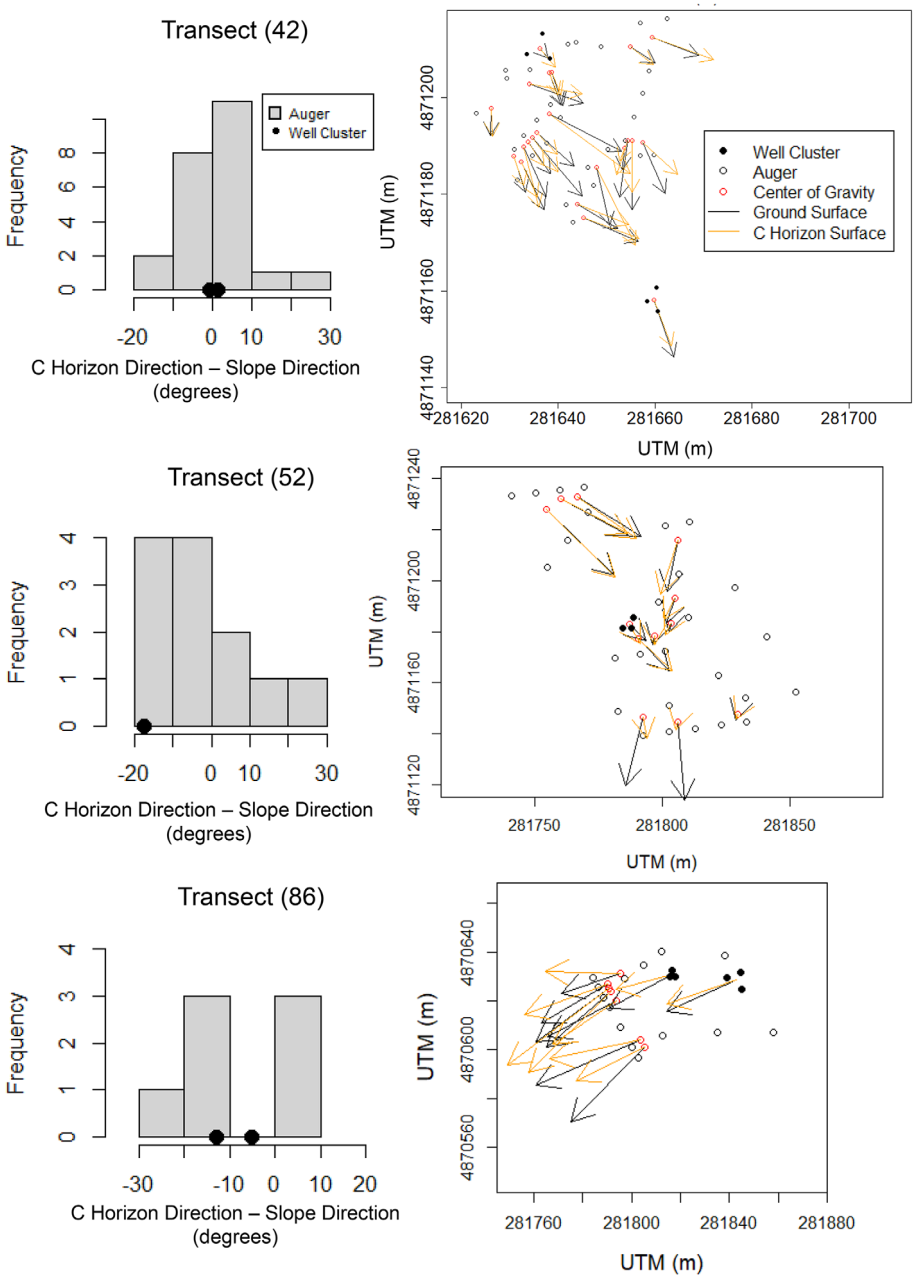

FIGURE 6 A map showing the location of auger investigations, shallow wells, and surface slope directions derived from three-point gradient calculations in each transect. Slope directions are illustrated by vectors originating from the centroid of each three-point cluster where the directional component of vectors is opposite to the direction of maximum horizontal gradient (downslope) and the magnitude of vectors are scaled proportional to the maximum horizontal gradient. A frequency histogram is included summarizing the difference in slope direction between the ground surface and the top of the C horizon. Measurements from well clusters are included for comparison.

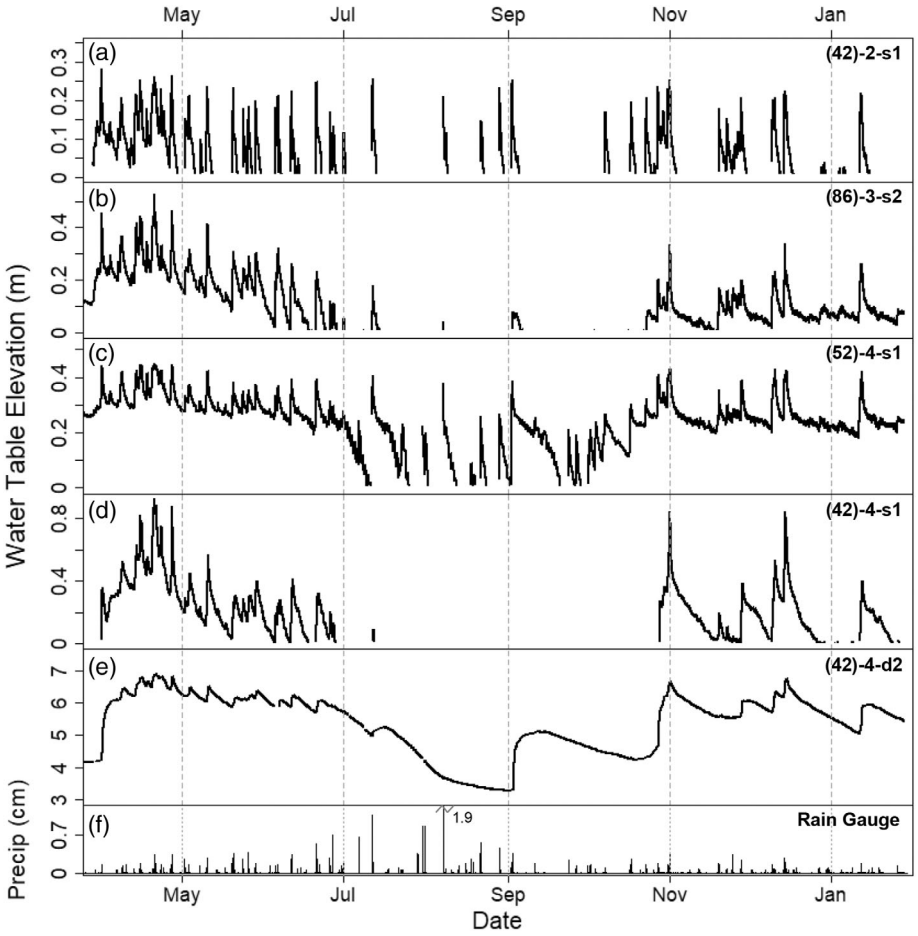

FIGURE 7 A time series (March 2019–Jan 2020) showing water table elevation relative to the ground surface ($y = 0$) for shallow wells (a–d), a deep well (e), and precipitation in cm/15-min (f). The gaps in data within the shallow wells (panels a–d) imply that the water table is below the base of the well. Well (42)-2-s1 is installed within the solum directly overlying bedrock while wells (86)-3-s2, (52)-4-s1 and (42)-4-s1 are installed within the solum overlying C horizon. Well (42)-4-d2 is screened entirely within the C horizon.

seasonally or on an event basis yet never dropping below the screened interval (Figure 7e). Near the ridges of the watershed, where bedrock outcrops close to the land surface and the solum is thin, water tables were episodic, only rising into the solum in response to rain or snow melt events (Figure 7a). Within thicker soils overlying the C horizon, water tables remained in the solum seasonally, dropping below the base of the solum in mid-summer (June–July) before rising back into the solum during the fall (Figure 7b–d). The highest water tables occurred during the spring snow melt season (March–April) that was followed by an overall recession period that persisted into the early summer (June–July; Figure 7).

Water table response to rainfall events was characterized by the time lag between maximum precipitation rates and the first occurrence of peak water table elevation for a given event. Precipitation rates are reported at 15-min logging intervals (Figures 7–12). Water table response across the well network varied depending upon transect, hillslope position, and soil horizon. For example, water tables within the solum in transects 42 and 86 exhibited longer time-lags in peak water table between different hillslope positions, while water tables within the solum in transect 52 occurred approximately at the same time regardless of hillslope position (Figure 8).

Within transect 42, the timing of peak water tables within the shallow wells was often delayed from each other on the order of hours (Figure 8), while the timing of peak water tables within deeper wells, installed in the C horizon, was delayed from those in the shallow wells on the order of days (Figure 9). In transect 86, the timing of peak water tables within the deeper wells was only delayed by a few hours from peak water table in the shallow wells (Figure 9). Water tables within shallow wells within each transect were flashier, responded sooner, and increased and receded at a faster rate than water tables within the C horizon (Figure 9).

3.4 | Groundwater flow direction, surface topography, and subsurface topography

Overall, the mean shallow groundwater flow direction followed the large-scale (i.e., on the order of 100 m) slope direction of land surface topography within WS3 (SE or SW; Table S1). For the southeast-facing slope, the mean surface slope direction and the mean groundwater flow direction for well clusters were 144 and 150 degrees azimuth, respectively. For the southwest facing slope, the mean surface slope direction and the mean groundwater flow direction for well clusters were 244 and 247 degrees azimuth, respectively. However, flow direction within a given cluster had a maximum range of 61 degrees and a minimum range of 10 degrees, and under certain conditions, flow direction showed deviations from the surface topography by as much as 56 degrees.

Although the overall direction of shallow groundwater flow mimicked the large-scale surface topography, changes in water table

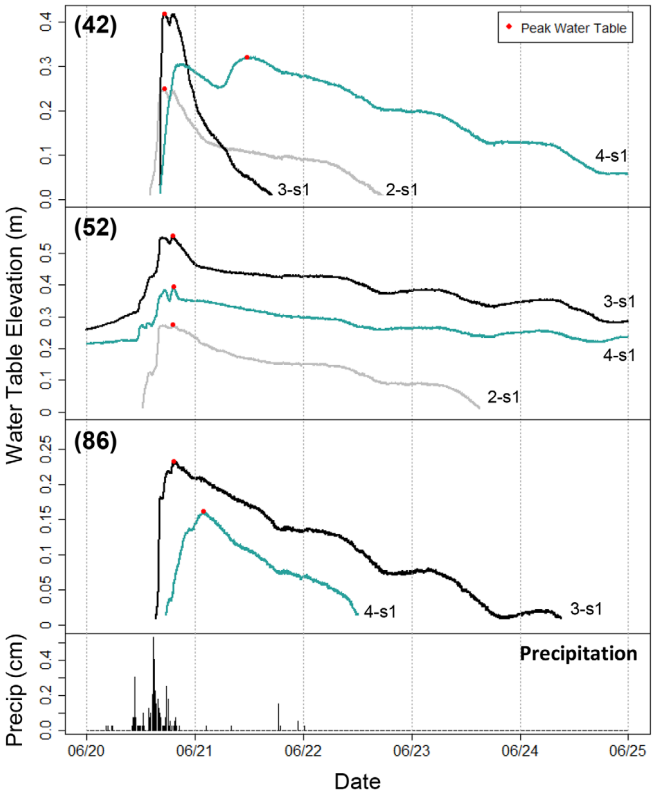

FIGURE 8 A time-series showing the response of water tables to a precipitation event within each transect (42, 52 & 86) at multiple hillslope positions (2-s1, 3-s1 & 4-s1). Peak water table is denoted with a red circle. Hillslope position 2-s1 is the furthest upslope within each transect while hillslope position 4-s1 is furthest downslope. Water tables are expressed as elevation above the base of the well ($y = 0$). See Figure 2 for transect and well locations.

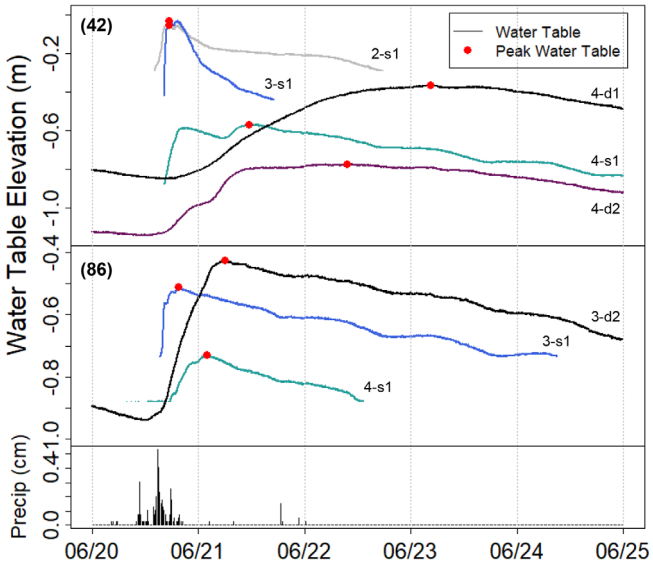

FIGURE 9 A time series showing water tables responding to a rain event in June, 2019 within both shallow and deep Wells at transects (42) and (86). Water tables are expressed as elevation relative to the ground surface ($y = 0$), and the peak water table is included to illustrate lag-times between each well (red points). See Figure 2 for transect and well locations. Wells 2-s1, 3-s1 and 4-s1 are shallow wells; 4-d1, 4-d2 and 3-d2 are deep wells.

elevation influenced the flow direction. During higher water tables, the direction of groundwater flow closely followed surface topography. However, as water tables receded, the flow direction deviated from surface topography. Three examples are used to show these patterns. The first example is a well cluster (4c-1) from transect 52 (Figure 10). During higher water table regimes, both the hydraulic gradient and direction of flow were closer to the surface topography (Figure 10a,b). However, under lower water table regimes, the flow direction deviated from surface topography towards the slope direction of the top of the C horizon (Figure 10a,b). Flow directions calculated over time had a normal distribution with an arithmetic mean between the surface topography and the C horizon slope direction (Figure 10c).

In the second example from transect 86, shallow groundwater flow direction within well cluster 3-c1 showed similar trends as (52)-4-c1 in following surface topography under higher water tables, the top of the C horizon under lower water tables, and an arithmetic mean between the C horizon and the surface topography (Figure 11). Similar to the first example, the interquartile range (Figure S1) and highest probability of flow direction (Figure 11c) fell between the slope direction of the top of the C horizon and the ground surface, and these features constrained the range in flow direction observed at each well cluster (Figures 10 and 11).

In the third example from transect 42, shallow groundwater flow direction within well cluster 4-c1 followed surface topography under higher water tables; however, it deviated from both the surface topography and the topography of the C horizon under lower water tables (Figure 12). The mean flow direction was offset from the ground surface by 6 degrees azimuth, and the slope direction of the ground surface was approximately equal to the slope direction of the surface of the C horizon (Figure 12c).

The relationship between shallow groundwater flow direction, surface topography and the top of the C horizon can be highlighted by examining a single event response in transect 86. Figure 13 shows the response of the water table in well cluster (86)-3-c1 immediately following a storm event, and the associated flow directions. At the beginning of the event (t_0) when water levels were lower, closer to the base of the well, the flow direction mimicked the top of the C horizon, and this trend continued until water levels begin to increase (t_1) in response to a precipitation event. As the water table height increased, flow direction deviated in the southward direction. As water table peaks (t_2) at approximately at 8 h after t_1, flow direction was within one degree of the surface topography gradient.

4 | DISCUSSION

4.1 | Shallow groundwater flow direction varies up to 60 degrees

Shallow groundwater flow in the critical zone of this glaciated headwater catchment exhibited substantial variations in both flow

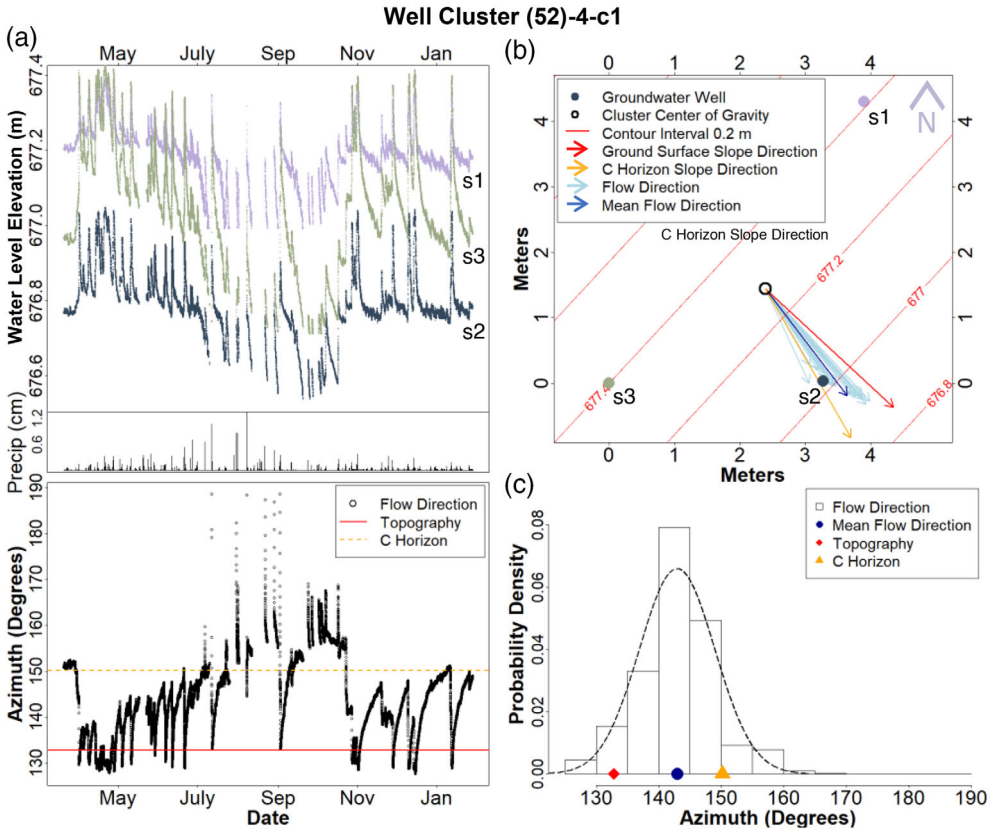

FIGURE 10 (a): Time series showing water level elevation, precipitation and groundwater flow direction (in azimuth) for well cluster (52)-4-c1 (see Figure 2 for location). Missing data within the time-series reflects the lack of sufficient water levels (in all three wells) needed for gradient calculations (b): Map view of the well cluster showing the variability in groundwater flow direction (blue vectors) in relation to the slope direction of the ground surface (red vectors) and the top of the C horizon (yellow vectors). The magnitude (length) of each vector is scaled proportional to the horizontal hydraulic gradient. (c): Probability density histogram summarizing groundwater flow direction with the slope direction of surface topography and the top of the C horizon. The dashed line is the normal distribution corresponding to the sample mean and standard deviation.

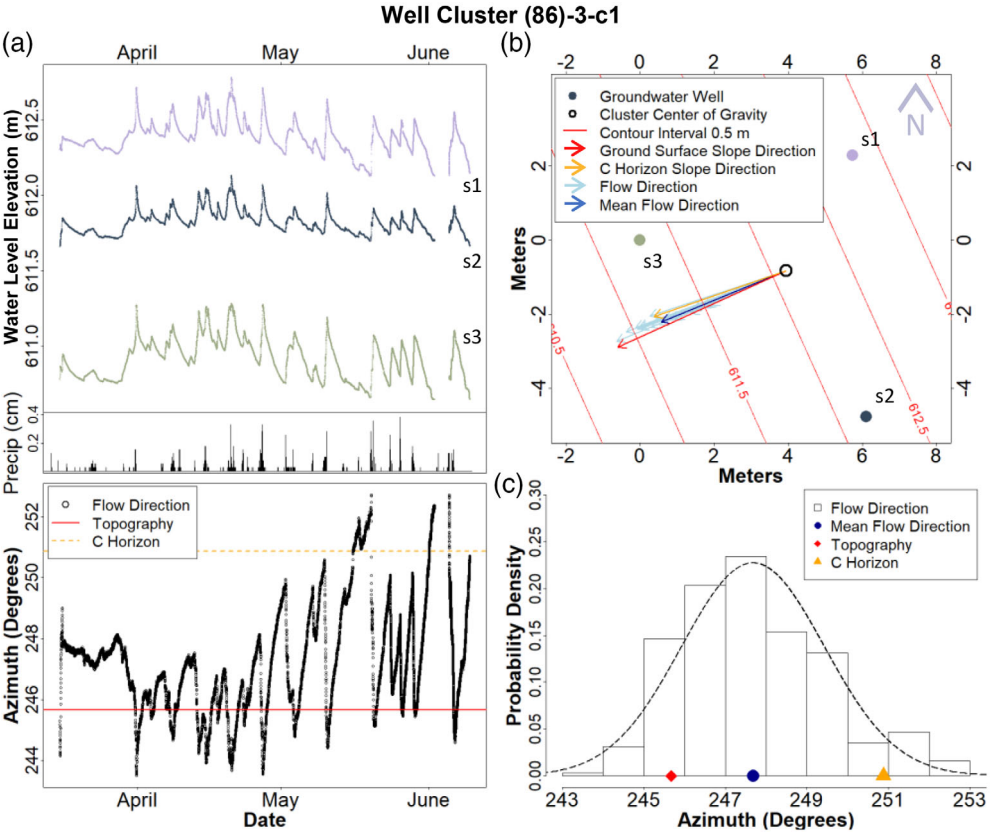

FIGURE 11 (a): Time series showing water level elevation, precipitation, and groundwater flow direction for well cluster (86)-3-c1. Missing data within the time-series reflects the lack of sufficient water levels (in all three wells) needed for gradient calculations (b): Map view of the well cluster showing the variability in groundwater flow direction (blue vectors) in relation to the slope direction of the ground surface (red vectors) and the top of the C horizon (yellow vectors). The magnitude (length) of each vector is scaled proportional to the horizontal hydraulic gradient. (c): Probability density histogram summarizing groundwater flow direction with the slope direction of surface topography and the top of the C horizon. The dashed line is the normal distribution corresponding to the sample mean and standard deviation.

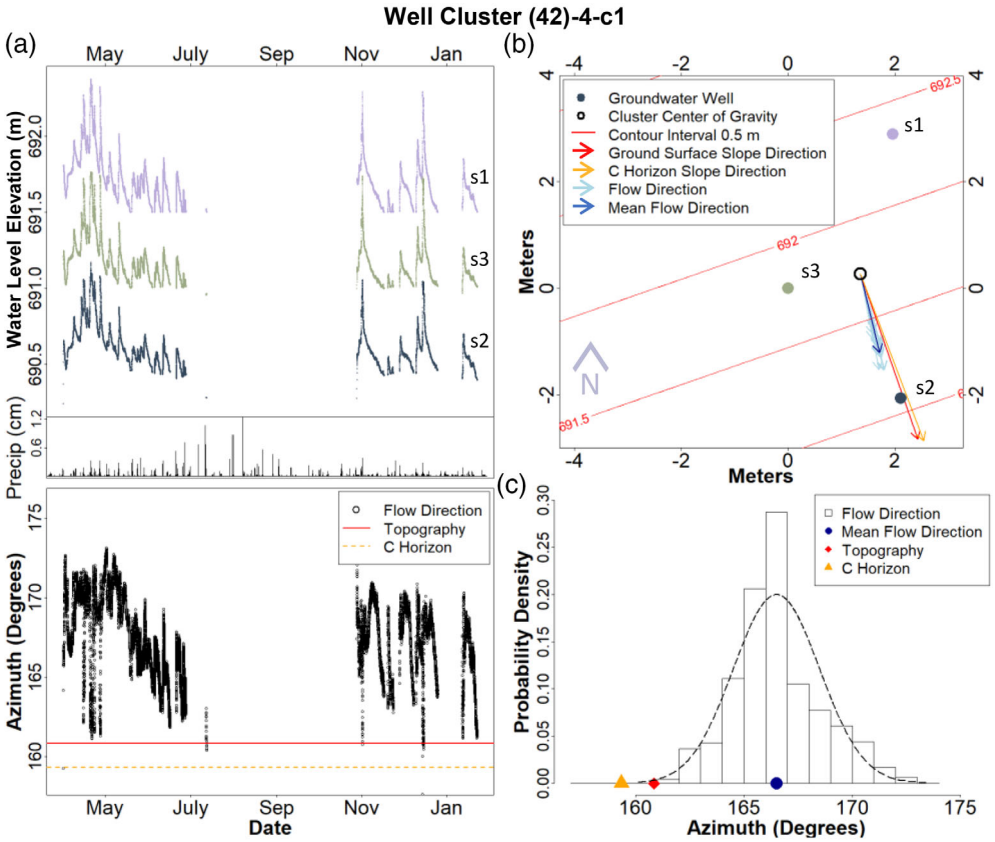

FIGURE 12 (a): Time series showing water level elevation, precipitation, and groundwater flow direction for a well cluster (42)-4-c1. Missing data within the time-series reflects the lack of sufficient water levels (in all three wells) needed for gradient calculations. (b): A map view of the well cluster showing the variability in groundwater flow direction (blue vectors) in relation to the slope direction of the ground surface (red vectors) and the top of the C horizon (yellow vectors). The magnitude (length) of each vector is scaled proportional to the horizontal hydraulic gradient. (c): A probability density histogram summarizing groundwater flow direction with the slope direction of surface topography and the top of the C horizon. The dashed line is the normal distribution corresponding to the sample mean and standard deviation.

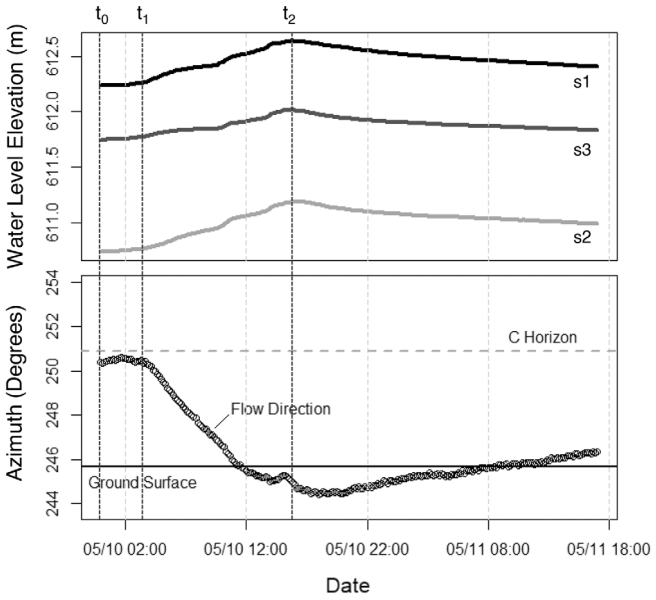

FIGURE 13 A time-series of water levels responding to a precipitation event in early May 2019 with the calculated flow direction at 10-min intervals in cluster (86)-3-c1. The beginning of the event (t_0), time of water level response (t_1), and the peak water level (t_2) are marked by dashed vertical lines. The slope direction of the ground surface and top of the C horizon is also included for comparison. Water levels are expressed in elevation relative to mean sea level.

direction and magnitude. The total range of groundwater flow direction over the monitoring period within the solum was greater than 60 degrees in some locations (52-4-c1, Table S1) but was less than 10 degrees in other locations (42-4-c1, Table S1). The shifts in flow direction occurred over short time scales (hours to days) on an event basis (Figure 13) and exhibited longer time-scale seasonal patterns as water table elevations decrease during the summer months and rise during the fall, winter and spring months (Figure 10–12). Both short-term and seasonal patterns in hydraulic gradients presented within study have direct implications for delineating groundwater flow paths in the critical zone as lateral subsurface stormflow becomes an important contributor to streamflow generation (Kienzler & Naef, 2008; Peters et al., 1995; Weiler et al., 2006).

Results from this study showed more variability in the range of groundwater flow direction within the upper hillslopes of WS3 (9–60 degrees) compared with those reported in other studies (<30 degrees) Rodhe & Seibert, 2011; Von Freyberg et al., 2014). This difference may be due to the focus in prior research investigating groundwater flow direction in headwater catchments on characterizing hillslope-streamflow connectivity (Tromp-van Meerveld et al., 2015; Vidon & Smith, 2007) with the majority of observations constrained to foot- and toe-slopes and riparian zones, and considerably fewer observations in the upper hillslopes. Groundwater flow within riparian zones is heavily influenced by streamflow stage (Rodhe & Seibert, 2011; Vidon & Smith, 2007), which may override any effect that permeability contrasts have on flow direction (the focus of this study).

4.2 | Shallow groundwater flow direction follows surface topography under high-water tables and the C horizon topography under low water tables

Permeability contrasts between the solum and underlying parent materials influence the distribution of energy potential. The C horizon in WS3 had a statistically significantly lower permeability than the solum; the interquartile range of K_{sat} within the C horizon was two orders of magnitude lower than the interquartile range of K_{sat} within the solum (Figure 4). For most locations within this study, the mean and interquartile range of flow direction observations were confined between the slope direction of the land surface and the slope direction of the C horizon (Figures 10 and 11, Table S1). Overall, these results are consistent with Tromp-van Meerveld et al. (2015) and Hutchinson and Moore (2000), who found that groundwater flow direction correlated with subsurface topography of confining units during lower water tables but followed surface topography during higher water tables. Tromp-van Meerveld et al. (2015) observed the largest standard deviation in hillslope flow directions within well clusters located in a bedrock hollow where the bedrock surface deviated from surface contours, and smaller deviation in hillslope flow directions where the bedrock surface followed surface topography. Similarly, the largest standard deviation in flow direction measured in this study, 52-4-c1, coincided with the largest difference in slope direction of C horizon topography from surface topography (Table S1). Our results suggest that the land surface topography and the top of the C horizon act as end members defining the upper and lower bounds of flow direction variability. Therefore, knowledge of C horizon topography may provide a constraint for characterizing the range of directions of event-based shallow groundwater flow.

The C horizon in our field area was texturally heterogenous and can have zones of higher permeability (Bailey et al., 2014) due to the presence of sand lenses that, if present, may not result in a decrease in permeability at the interface between the solum and C horizon. Additionally, the interface between the C horizon and the solum can be gradual and will not necessarily correspond to abrupt changes in hydraulic properties. This spatial heterogeneity in the hydraulic properties of glacial sediments comprising both the C horizon and solum makes it difficult to generalize hydraulic behaviour observed at the smaller, subcatchment scale for the entire catchment of WS3. Additionally, this heterogeneity may explain why the deviation in flow direction at some locations in this study do not correlate with C horizon topography (Figure 12).

Results from our catchment-scale auger investigation showed that the deviation of subsurface topography from surface topography observed at each well cluster can be generalized and falls within a range of deviations observed at the larger scale (Figure 6). Therefore, variability in flow direction may also be generalized at the hillslope scale using methods presented within this study, assuming that permeability contrasts are continuous.

Based on the results of this work, we present a simple conceptual model (Figure 14) for shallow groundwater flow direction within the solum changing in response to rising water table conditions immediately following a recharge event. This conceptual model assumes that a permeability contrast is present at the interface between the solum and the C horizon and applies to 1) water tables rising from the deeper groundwater system into the solum or 2) perched saturation developing within the upper C horizon rising into the solum (e.g., Klaus & Jackson, 2018). In scenario 1, at an early time-step immediately following a precipitation event (t_1) saturation rises from the deeper groundwater flow system into the solum. The higher permeability of the solum increases the lateral flux of water moving downslope (transmissivity feedback; see Kendall et al., 1999), therefore decreasing the rate of water table rise above the interface between the solum and C horizon. This leads to water table configurations mimicking the topography of the C horizon as the soil drains laterally. In scenario 2, at t_1 perched saturation develops at the base of the solum directly above the impeding C horizon, causing water tables to mimic the C horizon. Applicable to both scenarios, as conditions continue to wet up, water tables connect spatially across the landscape and flow direction shifts towards the direction of the land surface (t_2) implying an increase in hydrologic connectivity between saturated zones (Ambroise, 2004; Detty & McGuire, 2010b; Tromp-van Meerveld & McDonnell, 2006).

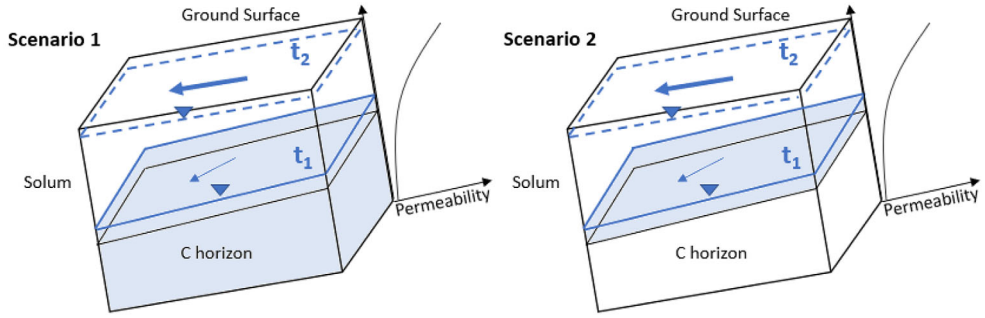

FIGURE 14 A conceptual model showing rising water tables in response to a recharge event. Scenario 1 shows a water table rising from within the C horizon, and Scenario 2 shows the development of perched saturation on top of the C horizon. In both scenarios the C horizon surface slopes away from surface topography, and there is a nonlinear decrease in permeability with depth. The solid blue line represents the water table at an earlier timestep (t_1) following the slope direction of the C horizon while the dashed blue line represents the water table at a later time step (t_2) following the slope direction of the ground surface.

4.3 | Implications for using surface topography as an approximation for hydraulic gradients

Due to the availability of land surface DEM data, it is common practice within modelling-based hydrologic studies in headwater catchments to use the land surface as an approximation of hydraulic gradient magnitude (Beven, 1997; Nippgen et al., 2015; Wigmosta et al., 1994). The widely used topographically driven rainfall-runoff model, TOPMODEL (Beven, 1997; Beven & Kirkby, 1979), uses the slope of the land surface to calculate topographic wetness indices (TWI) as a steady-state approximation of groundwater dynamics at each point within the catchment. Another widely used rainfall-runoff model is the distributed hydrologic soil vegetation model (Wigmosta et al., 1994), which approximates subsurface hydrologic gradients with land surface topographic gradients and thus routes subsurface water according to the surface topography. The schemes from these models are adapted and used in a host of other hydrologic models (e.g., Kuppel et al., 2018; Tague & Band, 2004; Vivoni et al., 2007). Previous experimental (field-based) investigations at WS3 have also used surface topographic gradients surrounding a single well as an approximation for subsurface hydraulic gradients in soils to investigate the response of subsurface fluxes to catchment storage dynamics (Detty & McGuire, 2010a; Gannon et al., 2014).

In this study, we observed dynamic changes in the magnitude of hydraulic gradients in response to changing water table elevation (Figures 10–12, Figure S1). Within some locations, the magnitude of the hydraulic gradient, and subsequently, the hydrologic flux, decreased as water table elevation decreased (52-4-c1 & 42-4-c1, Figures 10 and 11, Figure S1), suggesting that using surface topography as an approximation for water table gradients at these locations would produce an overestimation of subsurface hydrologic fluxes during dry periods. In contrast, at some other locations, the magnitude of the hydraulic gradient and hydrologic flux increased with decreasing water table elevations below a threshold; above the threshold, the patterns showed increases in gradient/flux with water table (86-4-c1, Figure S1). Overall, our results show that the magnitude of the hydraulic gradient can deviate from the maximum slope of the land surface by as much as 0.11 m/m at this site. Thus, the assumption that the hydraulic gradient can be approximated by surface topography may result in significant errors. Camporese et al. (2019) demonstrated that the standard land surface-based topographic wetness index (TWI) was a poor indicator of water table dynamics at the Panola Mountain Research Watershed, GA while a TWI calculated from subsurface bedrock topography was significantly better at predicting the development of saturated zones in response to recharge events. Likewise, other studies have shown that the soil-bedrock interface and its topographic characteristics are critical in explaining subsurface flow and saturation development (e.g., Graham et al., 2010; Lanni et al., 2013; Liang & Chan, 2017; Lin et al., 2006). Results of our study highlight the need for the characterization and establishment of a functional relationship between water table elevation and hydraulic gradients within the solum to improve estimation of the temporal dynamics of hydrologic fluxes. Additional research that considers the co-evolution of hydrological processes with structure of the critical zone (Troch et al., 2015) and pedogenesis (Van der Meij et al., 2018) is needed.

5 | CONCLUSIONS

In this study we observed the temporal behaviour of shallow groundwater flow direction within soils at five different hillslope positions in a glaciated headwater catchment (WS3) at the Hubbard Brook Experimental Forest. Through high-frequency water table measurements collected across a 10-month period, we determined that groundwater flow direction changes over short time scales, but also exhibited long term patterns. We showed that variability in flow direction was influenced by both surface topography and the subsurface topography of lower permeability units (C horizon). During wetter (high-water table) conditions, groundwater flow direction followed surface topography while under drier (lower water table) conditions, groundwater flow direction dominantly followed topography of the C horizon. Additionally, we showed that deviations in groundwater flow direction may be generalizable at the hillslope scale if soil unit depths and thicknesses are known. Our work demonstrates that knowledge of the topography (thickness and elevation) of subsurface soil units, especially lower permeability units, and the spatiotemporal patterns of water table dynamics can constrain estimates of the magnitude and direction of shallow groundwater flow in the critical zone of headwater catchments.

ACKNOWLEDGEMENTS

This project was supported by the National Science Foundation Division of Earth Sciences (1643327), NSF Division of Environmental Biology Hubbard Brook LTER program (1637685), and the Department of Geosciences at Virginia Tech. We thank the Hubbard Brook lateral weathering research group, including Scott Bailey, Brian Strahm, Don Ross, Amanda Pennino, Jennifer Bower, Stephanie Duston, Nathanial Rasnake, Delaney Peterson, Michaela Kuhn, Kinsey Ashe and JP Gannon, for many discussions, field assistance and support of this work.

DATA AVAILABILITY STATEMENT

The water level dataset collected during and/or analysed during this study is available in the Virginia Tech data repository (Benton et al., 2022).

ORCID

Joshua R. Benton https://orcid.org/0000-0002-1698-6455
Kevin J. McGuire https://orcid.org/0000-0001-5751-3956
Madeline E. Schreiber https://orcid.org/0000-0002-1858-7730

REFFERENCES

Ambroise, B. (2004). Variable "active" versus "contributing" areas or periods: A necessary distinction. *Hydrological Processes*, *18*(6), 1149–1155.

Bailey, A. S., Hornbeck, J. W., Campbell, J. L., & Eagar, C. (2003). *Hydrometeorological database for Hubbard Brook Experimental Forest: 1955–2000. General Technical Report NE-305* (p. 36). U.S. Department of Agriculture, Forest Service.

Bailey, S. W., Brousseau, P. A., McGuire, K. J., & Ross, D. S. (2014). Influence of landscape position and transient water table on soil development and carbon distribution in a steep, headwater catchment. *Geoderma*, *226–227*(1), 279–289. https://doi.org/10.1016/j.geoderma.2014.02.017

Bailey, S. W., McGuire, K. J., Ross, D. S., Green, M. B., & Fraser, O. L. (2019). Mineral weathering and podzolization control acid

neutralization and streamwater chemistry gradients in upland glaciated catchments, northeastern United States. *Frontiers in Earth Science*, *7*(4), 1–18. https://doi.org/10.3389/feart.2019.00063

Benton, J., McGuire, K., & Schreiber, M. (2022). Water level time series data for shallow groundwater within soils and glacial drift at the Hubbard Brook Experimental Forest, Woodstock, NH. *University Libraries, Virginia Tech*. Dataset. https://doi.org/10.7294/20532162

Beven, K. (1997). TOPMODEL: A critique. *Hydrological Processes*, *11*, 1069–1085. https://doi.org/10.1002/(SICI)1099-1085(199707)11:9

Beven, K. J., & Kirkby, M. J. (1979). A physically based, variable contributing area model of basin hydrology. Un modèle à base physique de zone d'appel variable de l'hydrologie du bassin versant. *Hydrological Sciences Bulletin*, *24*, 43–69. https://doi.org/10.1080/02626667909491834

Blumstock, M., Tetzlaff, D., Dick, J. J., Nuetzmann, G., & Soulsby, C. (2016). Spatial organization of groundwater dynamics and streamflow response from different hydropedological units in a montane catchment. *Hydrological Processes*, *30*, 3735–3753. https://doi.org/10.1002/hyp.10848

Bresciani, E., Goderniaux, P., & Batelaan, O. (2016). Hydrogeological controls of water table-land surface interactions. *Geophysical Research Letters*, *43*(18), 9653–9661. https://doi.org/10.1002/2016GL070618

Burns, M. A. (2012). *The Hydrological and Geochemical Role of the C Horizon in a Glacial Till Mantled Headwater Catchment*. University of Maine.

Camporese, M., Paniconi, C., Putti, M., & McDonnell, J. J. (2019). Fill and spill hillslope runoff representation with a Richards equation-based model. *Water Resources Research*, *55*(11), 8445–8462. https://doi.org/10.1029/2019WR025726

R Core Team. (2020). *R: A language and environment for statistical computing*. R Foundation for Statistical Computing. https://www.R-project.org/

Detty, J. M., & McGuire, K. J. (2010a). Threshold changes in storm runoff generation at a till-mantled headwater catchment. *Water Resources Research*, *46*(7), 1–15. https://doi.org/10.1029/2009WR008102

Detty, J. M., & McGuire, K. J. (2010b). Topographic controls on shallow groundwater dynamics: Implications of hydrologic connectivity between hillslopes and riparian zones in a till mantled catchment. *Hydrological Processes*, *24*(16), 2222–2236. https://doi.org/10.1002/hyp.7656

Emanuel, R. E., Hazen, A. G., McGlynn, B. L., & Jencso, K. G. (2014). Vegetation and topographic influences on the connectivity of shallow groundwater between hillslopes and streams. *Ecohydrology*, *7*(2), 887–895.

Erdbrügger, J., van Meerveld, I., Bishop, K., & Seibert, J. (2021). Effect of DEM-smoothing and -aggregation on topographically-based flow directions and catchment boundaries. *Journal of Hydrology*, *602*. https://doi.org/10.1016/j.jhydrol.2021.126717

Frei, S., Lischeid, G., & Fleckenstein, J. H. (2010). Effects of micro-topography on surface-subsurface exchange and runoff generation in a virtual riparian wetland - a modeling study. *Advances in Water Resources*, *33*(11), 1388–1401. https://doi.org/10.1016/j.advwatres.2010.07.006

Gannon, J. P., Bailey, S. W., & McGuire, K. J. (2014). Organizing groundwater regimes and response thresholds by soils: A framework for understanding runoff generation in a headwater catchment. *Water Resources Research*, *50*, 1–17. https://doi.org/10.1002/2014WR015498

Gillin, C. P., Bailey, S. W., McGuire, K. J., & Prisley, S. P. (2015). Evaluation of lidar-derived DEMs through terrain analysis and field comparison. *Photogrammetric Engineering and Remote Sensing*, *81*(5), 387–396. https://doi.org/10.14358/PERS.81.5.387

Graham, C. B., Woods, R. A., & McDonnell, J. J. (2010). Hillslope threshold response to rainfall:(1) a field based forensic approach. *Journal of Hydrology*, *393*(1–2), 65–76.

Harpold, A. A., Lyon, S. W., Troch, P. A., & Steenhuis, T. S. (2010). The hydrological effects of lateral preferential flow paths in a glaciated watershed in the northeastern USA. *Vadose Zone Journal*, *9*(2), 397–414. https://doi.org/10.2136/vzj2009.0107

Haught, D. R. W., & Tromp-van Meerveld, H. J. (2011). Spatial variation in transient water table responses: Differences between an upper and lower hillslope zone. *Hydrological Processes*, *25*(25), 3866–3877. https://doi.org/10.1002/hyp.8354

Hinton, M. J., Schiff, S. L., & English, M. C. (1993). Physical properties governing groundwater flow in a glacial till catchment. *Journal of Hydrology*, *142*(1–4), 229–249. https://doi.org/10.1016/0022-1694(93)90012-X

Hooper, R. P., & Shoemaker, C. A. (1986). A comparison of chemical and isotopic hydrograph separation. *Water Resources Research*, *22*(10), 1444–1454.

Hornbeck, J. W., Pierce, R. S., & Federer, C. A. (1970). Streamflow changes after forest clearing in New England. *Water Resources Research*, *6*(4), 1124–1132.

Hutchinson, D. G., & Moore, R. D. (2000). Throughflow variability on a forested hillslope underlain by compacted glacial till. *Hydrological Processes*, *14*(10), 1751–1766. https://doi.org/10.1002/1099-1085

Hvorslev, M. (1951). *Time Lag and Soil Permeability in Ground-Water Observations*. Corps of Engineers.

Inamdar, S. P., & Mitchell, M. J. (2007). Contributions of riparian and hillslope waters to storm runoff across multiple catchments and storm events in a glaciated forested watershed. *Journal of Hydrology*, *341*((1–2)), 116–130. https://doi.org/10.1016/J.Jhydrol.2007.05.007

Kendall, K. A., Shanley, J. B., & McDonnell, J. J. (1999). A hydrometric and geochemical approach to test the transmissivity feedback hypothesis during snowmelt. *Journal of Hydrology*, *219*(3–4), 188–205. https://doi.org/10.1016/S0022-1694(99)00059-1

Kienzler, P. M., & Naef, F. (2008). Temporal variability of subsurface stormflow formation. *Hydrology and Earth System Sciences*, *12*, 257–265. https://doi.org/10.5194/hess-12-257-2008

Klaus, J., & Jackson, C. R. (2018). Interflow is not binary: A continuous shallow perched layer does not imply continuous connectivity. *Water Resources Research*, *54*(9), 5921–5932.

Kuppel, S., Tetzlaff, D., Maneta, M. P., & Soulsby, C. (2018). EcH$_2$O-iso 1.0: Water isotopes and age tracking in a process-based, distributed ecohydrological model. *Geoscientific Model Development*, *11*, 3045–3069. https://doi.org/10.5194/gmd-11-3045-2018

Lanni, C., McDonnell, J., Hopp, L., & Rigon, R. (2013). Simulated effect of soil depth and bedrock topography on near-surface hydrologic response and slope stability. *Earth Surface Processes and Landforms*, *38*(2), 146–159.

Liang, W. L., & Chan, M. C. (2017). Spatial and temporal variations in the effects of soil depth and topographic wetness index of bedrock topography on subsurface saturation generation in a steep natural forested headwater catchment. *Journal of Hydrology*, *546*, 405–418.

Likens, G. E. (2013). *Biogeochemistry of a Forested Ecosystem* (3rd ed.). Springer.

Likens, G. E., Bormann, F. H., Johnson, N. M., Fisher, D. W., & Pierce, R. S. (1970). Effects of Forest cutting and herbicide treatment on nutrient budgets in the Hubbard brook watershed-ecosystem. *Ecological Monographs*, *40*, 23–47. https://doi.org/10.2307/1942440

Lin, H. S., Kogelmann, W., Walker, C., & Bruns, M. A. (2006). Soil moisture patterns in a forested catchment: A hydropedological perspective. *Geoderma*, *131*(3–4), 345–368.

Maier, F., van Meerveld, I., Greinwald, K., Gebauer, T., Lustenberger, F., Hartmann, A., & Musso, A. (2020). Effects of soil and vegetation development on surface hydrological properties of moraines in the Swiss Alps. *Catena*, *187*, 104353.

Maier, F., van Meerveld, I., & Weiler, M. (2021). Long-term changes in runoff generation mechanisms for two proglacial areas in the Swiss Alps II: Subsurface flow. *Water Resources Research*, *57*, e2021WR030223. https://doi.org/10.1029/2021WR030223

Nippgen, F., McGlynn, B., & Emanuel, R. (2015). The spatial and temporal evolution of contributing areas. *Water Resources Research*, *51*, 4550–4573.

Nyberg, L. (1995). Water flow path interactions with soil hydraulic properties in till soil at Gårdsjön, Sweden. *Journal of Hydrology*, *170*(1–4), 255–275.

Penna, D., Mantese, N., Hopp, L., Dalla Fontana, G., & Borga, M. (2015). Spatio-temporal variability of piezometric response on two steep alpine hillslopes. *Hydrological Processes*, *29*(2), 198–211. https://doi.org/10.1002/hyp.10140

Peters, D. L., Buttle, J. M., Taylor, C. H., & LaZerte, B. (1995). Runoff production in a forested, shallow soil, Canadian shield basin. *Water Resources Research*, *31*(5), 1291–1304.

Rodhe, A., & Seibert, J. (2011). Groundwater dynamics in a till hillslope: Flow directions, gradients and delay. *Hydrological Processes*, *25*(12), 1899–1909. https://doi.org/10.1002/hyp.7946

Shanley, J. B., Hjerdt, K. N., McDonnell, J. J., & Kendall, C. (2003). Shallow water table fluctuations in relation to soil penetration resistance. *Groundwater*, *41*(7), 964–972.

Singha, K., & Navarre-Sitchler, A. (2022). The importance of groundwater in critical zone science. *Groundwater*, *60*, 27–34. https://doi.org/10.1111/gwat.13143

Smith, R. S., Moore, R. D., Weiler, M., & Jost, G. (2014). Spatial controls on groundwater response dynamics in a snowmelt-dominated montane catchment. *Hydrology and Earth System Sciences*, *18*, 1835–1856. https://doi.org/10.5194/hess-18-1835-2014,2014

Stieglitz, M., Shaman, J., McNamara, J., Engel, V., Shanley, J., & Kling, G. W. (2003). An approach to understanding hydrologic connectivity on the hillslope and the implications for nutrient transport. *Global Biogeochemical Cycles*, *17*(4). https://doi.org/10.1029/2003GB002041

Tague, C. L., & Band, L. E. (2004). RHESSys: Regional hydro-ecologic simulation system—An object-oriented approach to spatially distributed modeling of carbon, water, and nutrient cycling. *Earth Interactions*, *8*(19), 1–42.

Troch, P. A., Lahmers, T., Meira, A., Mukherjee, R., Pedersen, J. W., Roy, T., & Valdés-Pineda, R. (2015). Catchment coevolution: A useful framework for improving predictions of hydrological change? *Water Resources Research*, *51*, 4903–4922. https://doi.org/10.1002/2015WR017032

Tromp-van Meerveld, H. J., & McDonnell, J. J. (2006). Threshold relations in subsurface stormflow: 2. The fill and spill hypothesis. *Water Resources Research*, *42*, W02411. https://doi.org/10.1029/2004WR003800

Tromp-van Meerveld, H. J., Seibert, J., & Peters, N. E. (2015). Hillslope-riparian-stream connectivity and flow directions at the Panola Mountain research watershed. *Hydrological Processes*, *29*(16), 3556–3574. https://doi.org/10.1002/hyp.1050

Twidale, C. R. (1990). Weathering, soil development, and landforms. In C. G. Higgins & D. R. Coates (Eds.), *Groundwater Geomorphology—the Role of Subsurface Water in Earth-Surface Processes and Landforms* (pp. 29–50). Geological Society of America, Special Paper, 252, 1990.

Van der Meij, W. M., Temme, A. J., Lin, H. S., Gerke, H. H., & Sommer, M. (2018). On the role of hydrologic processes in soil and landscape evolution modeling: Concepts, complications and partial solutions. *Earth-Science Reviews*, *185*, 1088–1106.

van Verseveld, W. J., McDonnell, J. J., & Lajtha, K. (2009). The role of hillslope hydrology in controlling nutrient loss. *Journal of Hydrology*, *367*(3–4), 177–187.

Vidon, P., & Smith, A. P. (2007). Upland controls on the hydrological functioning of riparian zones in glacial till valleys of the Midwest. *Journal of the American Water Resources Association*, *43*(6), 1524–1539. https://doi.org/10.1111/j.1752-1688.2007.00125.x

Vivoni, E. R., Entekhabi, D., Bras, R. L., & Ivanov, V. Y. (2007). Controls on runoff generation and scale-dependence in a distributed hydrologic model. *Hydrology and Earth System Sciences*, *11*(5), 1683–1701.

Von Freyberg, J., Radny, D., Gall, H. E., & Schirmer, M. (2014). Implications of hydrologic connectivity between hillslopes and riparian zones on streamflow composition. *Journal of Contaminant Hydrology*, *169*(July), 62–74. https://doi.org/10.1016/j.jconhyd.2014.07.005

Weiler, M., McDonnell, J. J., Tromp-van Meerveld, I., & Uchida, T. (2006). Subsurface stormflow. In *Encyclopedia of Hydrological Sciences*. John Wiley and Sons.

Wigmosta, M. S., Vail, L. W., & Lettenmaier, D. P. (1994). A distributed hydrology-vegetation model for complex terrain. *Water Resources Research*, *30*(6), 1665–1679. https://doi.org/10.1029/94WR00436

Yager, R. M., Kauffman, L. J., Soller, D. R., Haj, A. E., Heisig, P. M., Buchwald, C. A., Westenbroek, S. M., & Reddy, J. E. (2019). *Characterization and Occurrence of Confined and Unconfined Aquifers in Quaternary Sediments in the Glaciated Conterminous United States* (p. 90). U.S. Geological Survey Scientific Investigations Report 2018–5091. https://doi.org/10.3133/sir20185091

Zimmer, M. A., Bailey, S. W., McGuire, K. J., & Bullen, T. D. (2013). Fine scale variations of surface water chemistry in an ephemeral to perennial drainage network. *Hydrological Processes*, *27*(24), 3438–3451. https://doi.org/10.1002/hyp.9449

Zimmer, M. A., & McGlynn, B. L. (2017). Ephemeral and intermittent runoff generation processes in a low relief, highly weathered catchment. *Water Resources*, *53*, 7055–7077. https://doi.org/10.1002/2016WR019742

SUPPORTING INFORMATION

Additional supporting information can be found online in the Supporting Information section at the end of this article.

How to cite this article: Benton, J. R., McGuire, K. J., & Schreiber, M. E. (2022). Subsurface permeability contrasts control shallow groundwater flow dynamics in the critical zone of a glaciated, headwater catchment. *Hydrological Processes*, *36*(9), e14672. https://doi.org/10.1002/hyp.14672